ISSN: 2581-4311
DOI: doi.org/10.30967/IJCRSET/Pereira-MV/195

URF PUBLISHERS
connect with research world

International Journal of Current Research in Science, Engineering & Technology

https://urfpublishers.com/journal/ijcrset

Vol: 8 & Iss: 3

Research Article

Ultralong Fatigue Life Approach Based on Failure Diagrams

Corrêa JP[1], Alves JA[1], Teixeira MC[1], Albuquerque MJ[1], Yoshihara N[2] and Pereira MV[1]*

[1]Department of Chemical and Materials Engineering, Pontifical Catholic University of Rio de Janeiro - PUC-Rio, Rua Marquês de São Vicente, 225, Rio de Janeiro, 22451-900, RJ, Brazil

[2]Department of Mechanical Engineering, Pontifical Catholic University of Rio de Janeiro - PUC-Rio, Rua Marquês de São Vicente, 225, Rio de Janeiro, 22451-900, RJ, Brazil

Citation: Corrêa JP, Alves JA, Teixeira MC, Albuquerque MJ, Yoshihara N, et al., Ultralong Fatigue Life Approach Based on Failure Diagrams. *Int J Cur Res Sci Eng Tech* 2025; 8(3), 373-382. DOI: doi.org/10.30967/IJCRSET/Pereira-MV/195

Received: 30 August, 2025; **Accepted:** 10 September, 2025; **Published:** 15 September, 2025

***Corresponding author:** Pereira MV, Department of Chemical and Materials Engineering, Pontifical Catholic University of Rio de Janeiro – PUC-Rio, Rua Marquês de São Vicente, 225, Rio de Janeiro, 22451-900, RJ, Brazil

A B S T R A C T

The objective of this research was verifying the applicability of FADs diagrams, based on the stress equivalence models proposed by Goodman, Gerber and Soderberg, beyond their original frontiers (failures between 1×10^4 – 1×10^7 cycles); in other words, to evaluate the extension to very high cycle fatigue (VHCF) (failures after 1×10^7 cycles). A high strength structural steel and an aluminum alloy were used to perform cyclic tests and compare failure diagrams in long fatigue regime. The materials were tested with fully and partially reversible loads to determine their fatigue life under both conditions. FADs were plotted for both materials, comparing their finite and infinite life predictions in very high cycle fatigue. It was found that Goodman`s FAD provided the best experimental data fit for finite and infinite fatigue life predictions for both materials. However, the materials` microstructural characteristics showed a significant influence on the failure assessment in Gerber`s FAD as well as in Soderberg`s FAD. While Gerber`s FAD was well fitted for the experimental fatigue life data in terms of the aluminum alloy, Soderberg`s FAD was more suitable for the high strength structural steel.

Keywords: Mean stresses; Equivalent stress models; Very high cycle fatigue

Introduction

Fatigue damage refers to gradual degradation in structures and components under to cyclic loads during service operations[1]. In response, studies and research on fatigue failures are fundamental subjects to the industry, aiming to improve the safety and reliability of said structures and components during their design lives and moving away the undesirable fatigue failures while in service[2-7].

When considering non-random situations, the cyclic loads can be classified as fully or partially reversible. In fully reversible loads, the load ratio is -1 with a mean stress of zero, while in partially reversible loads, both parameters assume values other than -1 and zero[8,9]. The applied stress levels and the number of cycles to failure will determine the fatigue regime under which the material is tested[10,11]. Test stresses above the material's yield strength and a fatigue life less than 1E5 cycles characterize a low cycle fatigue regime. On the other hand, test stresses below the material's yield strength with a fatigue life between 1×10^5 – 1×10^7 cycles characterize a high cycle fatigue regime.

Until some years ago, due to the low frequency of past test equipment, which would considerably increase the testing time considerably, the concept of infinite fatigue life was well established and associated with a fatigue limit of 1×10^7 cycles, especially concerning ferrous materials. However, technological developments have resulted in new fatigue life approaches of mechanical and structural components that go beyond 1×10^7 cycles. Thus, the evaluation of the behavior of materials subjected to long or super-long fatigue life (1×10^8 – 1×10^{12} cycles) has become essencial for projects in different areas of engineering and medicine, creating the concept of very high cycle fatigue (VHCF) [12-15], in accordance with pioneering fatigue tests in ultrasonic equipment performed by Manson in 1950[16]. **(Figure 1)** shows the schematic design of an S-N curve for a material with a fatigue life beyond 1×10^7 cycles.

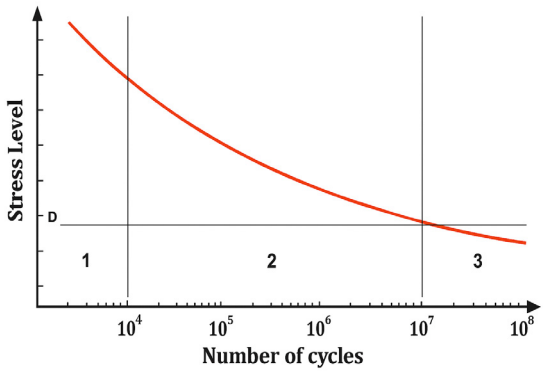

Figure 1: Schematic of an S-N curve with continuous failure beyond 1×10^7 cycles[10].

With ultrasonic testing, it has become feasible to study the performance of materials under extremely long fatigue regimes in reduced timeframes. For example, achieving 1×10^9 loading cycles in conventional fatigue equipment, which operates at a frequency of 100 Hz, would take about four months, while ultrasonic equipment operating at 20 kHz achieves the same number of cycles in just 14 hours[17]. Ultrasonic testing systems have different configurations from one laboratory to another, but preserve fundamental components, as illustrated in **(Figure 2)**[12]. In this figure, one can observe: (1) a power generator, responsible for converting the voltage signal from the electrical network, normally between 50 and 60 Hz, into a 20 Hz sinusoidal electrical signal; (2) a piezoelectric converter, excited by a sinusoidal electrical signal, which transforms the electrical pulse into longitudinal mechanical vibrations with the same frequency; (3) an ultrasonic horn, responsible for amplifying these vibrations until the maximum stress in the central cross section of the sample is reached; (4) a data acquisition system, which monitors and records the experimental parameters throughout the test.

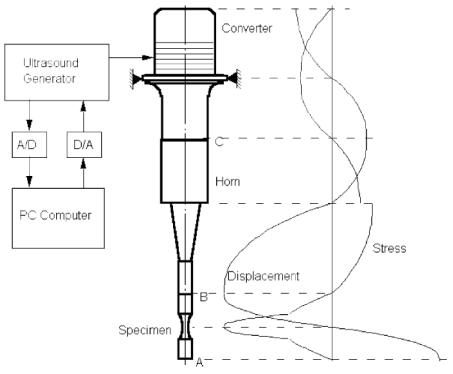

Figure 2: Schematic drawing of an ultrasonic machine[12].

According to the literature, several studies indicate that the fatigue life of metallic materials continues to decrease even after 1×10^7 loading cycles[18-29]. Bathias[12] observed the absence of an infinite life in ferrous materials such as AISI 4240 steel when reporting failures around 5.75×10^8 cycles. Nishijima, et al.[18] concluded that changes in fracture initiation sites occur over long lifetimes: as the number of cycles increases, the origin of the crack migrates from the surface to the interior of the material. The same behavior was also identified by Wang, et al,[19,20] when associating modification in the nucleation site with the presence of internal inclusions. In VHCF regimes, it is common for cracks to initiate in internal sites or just below the surface, usually in microstructural heterogeneities such as non-metallic inclusions[21]. This type of nucleation gives rise to a characteristic circular pattern on the fracture surface, known as fish-eye, with a refined morphology area in the center and near the inclusion. The terminology attributed to the fish-eye internal region can vary authors, reflecting different interpretations of its origin. Murakami, et al.[22,23] named it as optically dark area (ODA), highlighting the role of internal defects and hydrogen trapping in the formation of this zone, associated with subsurface nucleation. Sakai, et al.[24,25] use the term fine granular area (FGA), based on the presence of fine sub grains with distinct crystallographic orientations, formed during fatigue cycles. Making use of diffraction techniques to analyze fracture surfaces inside and outside the FGA, Sakai proposed that the formation mechanism is related to polygonization and micro displacements. Shiozawa, et al.[26,27] refer to this region as granular bright facet (GBF), having observed that internal cracks originate preferably in non-metallic inclusions, accompanied by fracture surfaces with granular brightness. Furuya, et al,[28] when conducting tests at frequencies up to 20 kHz, also found the occurrence of fatigue failures even after 1×10^9 cycles and demonstrated that the inclusion size impact significantly the fatigue resistance of the material. These results consistently reinforce that fatigue life does not stabilize with an increase in the number of cycles. On the contrary, it continues to decrease, being strongly influenced by internal microstructural factors.

Regarding fatigue life prediction of materials, for operational reasons, tests are usually performed under uniaxial loading, generally with a load ratio equal to -1[29]. An example of loading history with regards to the maximum ($\boldsymbol{\sigma}_{max}$) and minimum ($\boldsymbol{\sigma}_{min}$) stresses is presented in **(Figure 3)**. Based on $\boldsymbol{\sigma}_{max}$ and $\boldsymbol{\sigma}_{min}$, one can calculate the stress variation ($\boldsymbol{\Delta\sigma}$), mean stress ($\boldsymbol{\sigma}_m$), alternating stress($\boldsymbol{\sigma}_a$) and loading ratio (R) according to Equations 1-4, respectively.

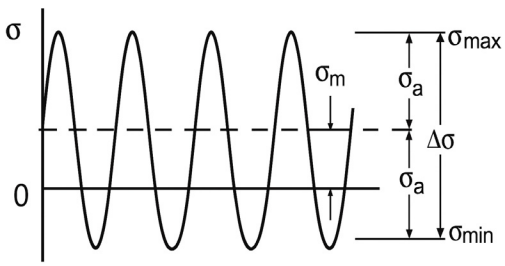

Figure 3: Loading history[9].

$$\Delta\sigma = \sigma_{max} - \sigma_{min} \qquad 1$$

$$\sigma_m = \frac{\sigma_{max} + \sigma_{min}}{2} \qquad 2$$

$$\sigma_a = \frac{\sigma_{max} - \sigma_{min}}{2} \quad 3$$

$$R = \frac{\sigma_{min}}{\sigma_{max}} \quad 4$$

However, the methodologies developed for fully reversible loading do not accurately predict the fatigue life of components subjected to mean stresses[30]. It is well known that mean tensile stresses tend to reduce the materials fatigue life, as it keeps the crack flanks open, facilitating their propagation. In contrast, mean compressive stresses promote crack closure, hindering the advancement of the crack[30]. At the end of the 19th century, the first studies on the effects of mean stresses appeared, mainly focusing on the evaluation of the durability of bridges[31,32]. As a result, Goodman[33], Gerber[34] and Soderberg[35] proposed independent methods to predict similar fatigue damages caused by combined (see Figure 2 and Equation 3) mean and alternating stresses, considering fully reversible load tests. The theories are based on several possible correlations between the limit stresses to reach fatigue life in the range of $1\times10^4 - 1\times10^7$ cycles, obtained by means of Wöhler curve or SN curve[36] and mean stresses, represented by mechanical properties of the material. In Goodman's proposal, the relationship between alternating and mean stresses is described by a straight line, with the mean stresses limited by the material's strength. In Gerber's approach, this relationship describes a parabola, with the same mean stress limit as Goodman. In turn, Soderberg's criterion admits a linear relationship between stresses, like Goodman, with the mean stress limit equivalent to the material's yield strength.

Haigh's diagram[37,38] addresses the Goodman, Soderberg and Gerber models in the context of failure analysis diagrams (FADs). FADs are considered fundamental approaches in engineering to assess the risk of failure of mechanical and structural components, by showing graphically distinguished regions of safety (not failure) and unsafety (failure). In Haigh's diagram, the straight lines of Goodman and Soderberg, as well as Gerber's parabola, constructed based on the material fatigue resistance, separate finite and infinite fatigue life, that mean failure and safe regions, respectively. The graph is constructed on a plane where the axes represent the relationship between alternating and mean stress. Each point on this plane corresponds to a possible combination of these stresses in mechanical components and structures. Points below the curves indicate safe load conditions and a theorical infinite fatigue life. On the other hand, points above the curves represent critical load conditions, indicating that the component may fail after a certain number of cycles. The Haigh diagram depicted in **(Figure 4)** was plotted based on Goodman Soderberg and Gerber curve equations[39-41], which correlate reversible and non-reversible test parameters, presented as Equations 5, 6 and 7, respectively.

$$\frac{\sigma_a}{\sigma_f} + \frac{\sigma_m}{\sigma_{uts}} = 1 \quad 5$$

$$\frac{\sigma_a}{\sigma_f} + \left(\frac{\sigma_m}{\sigma_{uts}}\right)^2 = 1 \quad 6$$

$$\frac{\sigma_a}{\sigma_f} + \frac{\sigma_m}{\sigma_{yield}} = 1 \quad 7$$

where σ_a and σ_m were previously defined, while σ_f, σ_{uts} and σ_{yield} represent limit stress to a given fatigue life in fully reversible loading, materials` ultimate tensile strength and materials` yield strength, respectively.

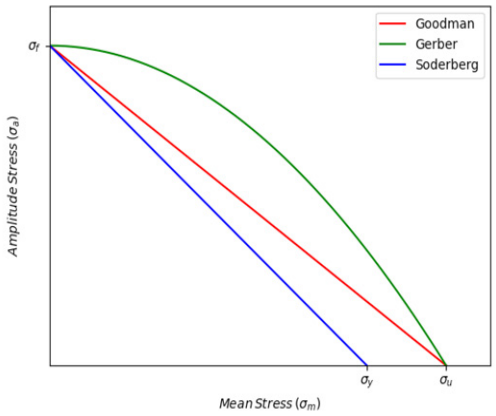

Figure 4: Haigh's theoretical diagram and equivalence curves[37].

Several studies have explored and improved the application of Haigh diagrams in fatigue analysis under different conditions. Bellows, et al.[42] validated the step test method for constructing Haigh diagrams in Ti-6Al-4V alloy, demonstrating the method efficiency for representing the material fatigue behavior under different mean stresses. Pallarés-Santasmartas, et al,[43] adopting the Haigh diagram, demonstrated the effect of mean stresses on the fatigue performance of quenched and tempered DIN 34CrNiMo6 steel, highlighting the significant influence of mean stress on the material fatigue resistance. Ponnapureddy, et al.[44] investigated the effects of creep on the high-cycle fatigue life in 617M nickel alloy, concluding that the interaction between creep and fatigue damages should be integrated into a unique Haigh diagram, to ensure greater reliability in the design of components subjected to cyclic loads and high temperatures simultaneously.

Experimental Procedure

Materials

Two metallic materials with different microstructures and mechanical properties were selected for this research: DIN 34CrNiMo6 high strength structural steel, quenched and tempered, with a tensile strength of 900 MPa; 6351 T6 aluminum alloy, heat-treated and artificially aged, with a tensile strength of 370 MPa. The chemical compositions of the materials were obtained by optical emission analysis according to ASTM A751-21[45] and E1251-24[46] standards and presented in **(Table 1)** and **(Table 2)**.

Table 1: Chemical composition of the DIN 34CrNiMo6 steel (% wt).

C	Cr	Mo	Ni	Fe
0.38	1.51	0.24	1.75	balance

Table 2: Chemical composition of the Al 6351 T6 alloy (% wt).

Mg	Fe	Cu	Mn	Zn	Ti	Si	Al
0.60	0.50	0.10	0.60	0.20	0.20	1.00	balance

Mechanical properties

(Table 3) lists the mechanical properties of both materials, obtained according to the standard tensile test ASTM E8/E8M-24 and ASTM E111-17[47,48], corresponding to the average value of three tests. Vickers' hardness was determined after three tests, using a load of 1 kgf applied for 10 s, according to the ASTM E384-22 standard[49].

Table 3: Mechanical properties.

Material	Young`s modulus (GPa)	0.2%-offset yield stress (MPa)	Ultimate tensile strength (MPa)	Vickers hardness (kgf/mm²)
DIN 34CrNiMo6	210	760	900	270
Al 6351 T6	69	270	370	105

Metallography

Samples for metallographic analysis were cut from specimens that have undergone fatigue testing and fractography analysis. The metallographic preparation was carried out in accordance with ASTM E3-11[50] standard; polishing was performed in stages using diamond paste (steel and aluminum alloy) and colloidal silica (aluminum alloy).

The chemical composition of the inclusions and precipitates was determined by energy-dispersive spectroscopy (EDS). Non-metallic inclusions (34CrNiMo6 steel) and precipitates or second-phase particles (6351-T6 aluminum alloy) were characterized in accordance with ASTM E1245-03 standard[51].

The analysis of inclusions, precipitates and second-phase particles was performed in five areas per specimen using ImageJ software, with scale calibration in µm/pixel. According to Murakami's classification, inclusions were categorized as superficial, subsurface or internal[4]. The size of each inclusion was determined based on the maximum and minimum Feret diameters obtained through image processing; the maximum Feret corresponds to the largest apparent length of the inclusion, while the minimum Feret represents the smallest orthogonal dimension. These measurements allowed the recording of the largest and smallest inclusion sizes in each analyzed area, ensuring accuracy and reproducibility of the data

Fatigue tests

The geometries of the VHCF specimens were designed based on Bathias' formulas[12] adopting densities of 7,870 kg/m³[52] and 2,710 kg/m³[53], for the steel and aluminum alloy, respectively. Regarding the tests under fully reversible loading, a thread was machined at one end of specimen's length, to fix the specimen in the equipment. However, for tests with partially reversible loading, a second thread was machined opposite to the first, making possible the attachment of a load cell to the specimen. The specimen geometries are presented in **(Figure 5)** and **(Figure 6)**.

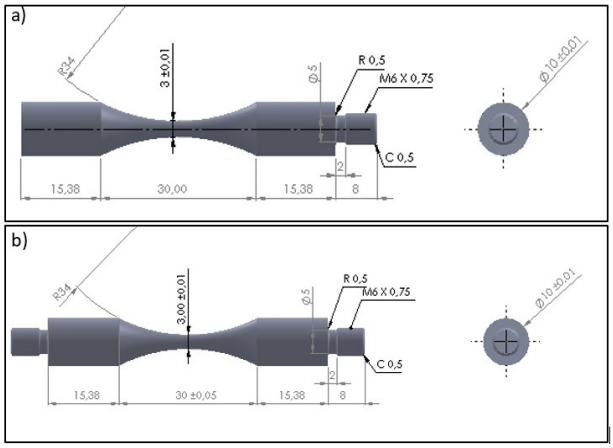

Figure 5: Geometries of the DIN34CrNiMo6 steel specimens: a) fully reversible loads; b) partially reversible loads.

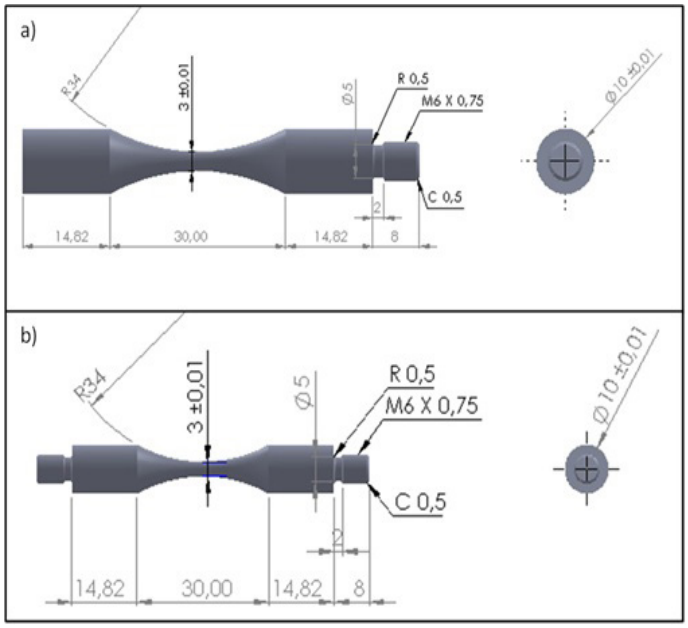

Figure 6: Geometries of the Al 6351 T6 alloy specimens: a) fully reversible loads; b) partially reversible loads.

VHCF tests were carried out at the Very High Cycle Fatigue Laboratory (LABFADAC) at PUC-RIO, making use of ultrasonic equipment. All tests were performed under uniaxial tensile/compression loading, at a frequency of 20 kHz adopting an intermittent pulse and pause of 200 ms each, combined with a constant flow of compressed air on the specimen to ensure thermal stability at 25 °C.

The first step of VHCF tests was carried out applying fully reversible loads (load ratio and mean stress equivalent to -1 and zero, respectively) to the specimens. Alternating stresses ranged from 0.35 to 0.60 of the ultimate tensile strength of the materials to ensure a long fatigue life (at least 1×10^9 cycles) under lower stress levels[54]. The stress ranges adopted for both materials are presented in **(Table 4)** and **(Table 5)**. The tests were conducted until the specimen failure or run out in 1.2×10^9 cycles and three specimens were tested at each stress for each material. **(Figure 7)** presents a DIN34CrNiMo6 steel specimen loaded in fully reversible condition.

Table 4: VHCF test stresses for DIN34CrNiMo6 steel under fully reversible loads.

σ_a (MPa)	$\frac{\sigma_a}{\sigma_{uts}}$ (%)
315	35
405	45
420	47
440	49
460	51
480	53
500	56
540	60

The second step of VHCF tests was performed with the specimens subjected to partially reversible loads (load ratio and mean stress different of -1 and zero, respectively). The specimens were preloaded by a load cell attached to their second thread, which induced tensile mean stress during the fatigue tests.

In order to evaluate the applicability of the Goodman, Soderberg and Gerber models to predict failures in the VHCF regime, different combinations of mean and alternating stresses were selected. Alternating stresses ranged from 0.30 to 0.50 of the ultimate tensile strength of the materials to ensure the fatigue life as longer as possible and the load ratios were selected as tensile/compression (-0.25 and -0.50) and fully tensile (0). In the sequence, the mean stresses were calculated using Equation 8.

Table 5: VHCF test stresses for Al 6351 T6 alloy under fully reversible loads.

σa **(MPa)**	$\frac{\sigma_a}{\sigma_{uts}}$ (%)
130	35
148	40
159	43
167	45
174	47
185	50
196	53
207	56

Figure 7: DIN34CrNiMO6 steel specimen under fully reversible loading.

$$\sigma_m = \sigma_a \frac{-1-R}{R-1} \qquad 8$$

where $\boldsymbol{\sigma}_m$, $\boldsymbol{\sigma}_a$ and R was previously defined. **(Table 6)** and **(Table 7)** indicate the stresses adopted for fatigue tests with partially reversible loading. In these tables, $\boldsymbol{\sigma}_{max}$ and $\boldsymbol{\sigma}_{min}$ represent the maximum and minimum values of test stresses, respectively. **(Figure 8)** presents a DIN 34CrNiMo6 steel specimen loaded in partially reversible condition.

Table 6: VHCF test stresses for DIN 34CrNiMo6 steel under partially reversible loads.

(%)	R	$\boldsymbol{\sigma}_a$ (MPa)	$\boldsymbol{\sigma}_m$ (MPa)	$\boldsymbol{\sigma}_{max}$ (MPa)	$\boldsymbol{\sigma}_{min}$ (MPa)
0.40	-0.50	360	120	480	-240
0.50		450	150	600	-300
0.40	-0.25	360	216	576	-144
0.45		400	240	640	-160
0.35	0	315	315	630	0
0.40		360	360	720	0

Table 7: VHCF test stresses for Al 6351 T6 alloy under partially reversible loads.

(%)	R	$\boldsymbol{\sigma}_a$ (MPa)	$\boldsymbol{\sigma}_m$ (MPa)	$\boldsymbol{\sigma}_{max}$ (MPa)	$\boldsymbol{\sigma}_{min}$ (MPa)
0.30	-0.50	111	37	148	-74
0.40		148	49	197	-99
0.30	-0.25	111	67	178	-44
0.40		148	89	237	-59
0.30	0	111	111	222	0
0.40		148	148	296	0

Figure 8: DIN 34CrNiMo6 steel specimen under partially reversible loading.

Results and Discussion

Metallography

Four metallographic specimens were analyzed, extracted from the fracture surfaces of the specimens that exhibited the longest fatigue lives: two from 6351-T6 aluminum alloy and two from DIN 34CrNiMo6 steel. For each material, one specimen corresponded to the sample subjected to fully reversed loading and the other to partially reversed loading.

Examples of the DIN 34CrNiMo6 steel and Al 6351-T6 alloy microstructures are presented in **(Figures 9 and 10)**. For each specimen, five microscopy images were acquired. Through digital image processing, the maximum and minimum length (Feret diameters) of the inclusions were determined in each image, enabling the registration of the largest and smallest sizes observed **(Table 8)**.

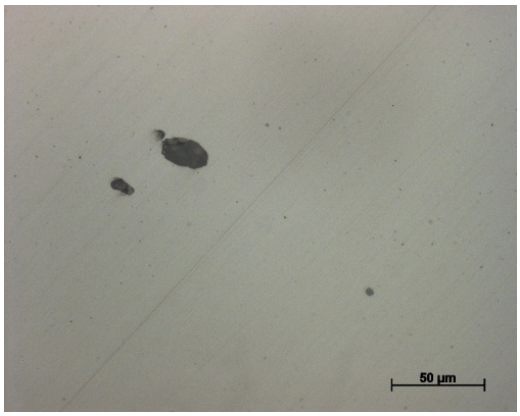

Figure 9: Optical micrograph of the DIN 34CrNiMo6 steel specimen (fully reversed loading).

Table 8: Maximum and minimum Feret diameters for both materials.

	Loading	Sample	Maximum inclusion (µm)	Minimum inclusion (µm)
DIN 34CrNiMo6	Fully reversed	1	22.1	0.3
		2	27.8	0.4
		3	13.3	1.3
		4	22.2	1.8
		5	27.2	2.7
	Partially reversed	1	36.7	2.7
		2	31.4	3.7
		3	18.3	2.4
		4	31.2	3.8
		5	28.4	0.3
Al 6351 T6	Fully reversed	1	10.5	0.1
		2	12.1	0.1
		3	10.3	1.0
		4	12.2	1.0
		5	10.1	1.3
	Partially reversed	1	13.3	1.1
		2	8.4	1.0
		3	7.7	17
		4	8.1	1.0
		5	12.3	0.1

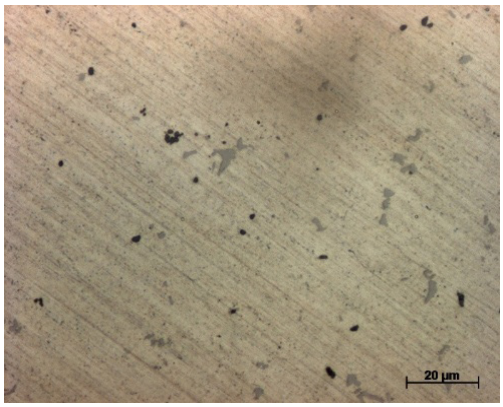

Figure 10: Optical micrograph of the 6351-T6 aluminum alloy specimen (partially reversed loading).

The results indicated that the most significant differences in inclusion size are associated with the type of material investigated. The DIN 34CrNiMo6 steel **(Figure 9)** exhibited substantially larger inclusions, with maximum Feret diameters approaching 36 µm, whereas the 6351-T6 aluminum alloy **(Figure 10)** displayed smaller inclusions, with maximum Feret diameters around 13 µm. These findings emphasize the predominant role of microstructure and inclusion size in governing the fatigue process.

Curve S-N

The results of fully reversed loading tests performed on both alloys to establish the VHCF fatigue life curves are presented in **(Figure 11)** and **(Figure 12)**.

In the case of the steel, fatigue fracture occurred at stress amplitudes corresponding to approximately 49% to 60% of $\boldsymbol{\sigma}_{uts}$, whereas for the aluminum alloy, fracture was observed between 35% and 52% of $\boldsymbol{\sigma}_{uts}$, both within a fatigue life range of 1×10^5 to 1.2×10^9 cycles.

The fits of the S-N curves yielded the Basquin coefficients. For the steel, parameters A and B were found to be 863 and -0.0370, respectively. For the aluminum alloy, the values were 404 and -0.0522, respectively. The Basquin relationships for both alloys are presented in Equations 9 and 10, respectively.

$$\sigma_a = 863N_f^{-0.0370} \qquad 9$$

$$\sigma_a = 404N_f^{-0.0522} \qquad 10$$

Probability bands were constructed to assess the theoretical results from the Basquin equations. A relationship between the theoretical fatigue life and the experimental life is presented in **(Figure 13)** and **(Figure 14)** for the steel and aluminum alloy, respectively. Scatter bands with a ratio of 1:2 was included in the relationship.

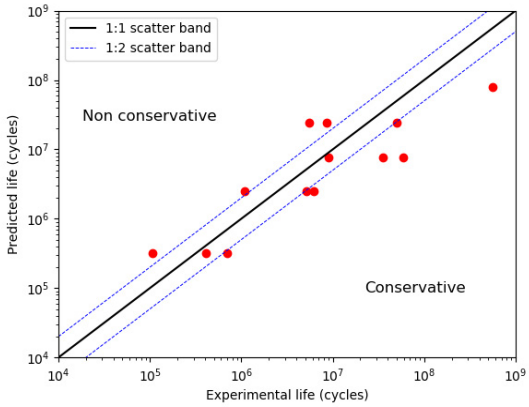

Figure 13: Experimental life vs. predicted life based on the S-N curve of DIN 34CrNiMo6.

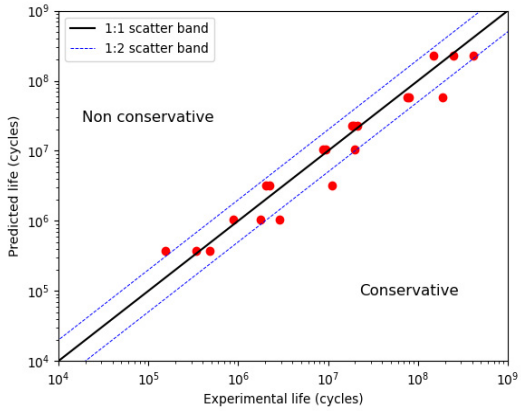

Figure 14: Experimental life vs. predicted life based on the S-N curve of Al 6351 T6.

The aluminum alloy exhibited most of its results within the scatter band, with few in the conservative region. The steel, in turn, had more dispersed results, which may have been affected by the presence of more significant defects.

Failure diagrams

Given a partially reversible loading, the Haigh-Soderberg failure diagram predicts failure or non-failure based on stress equivalence models. To achieve this scope, stresses ($\boldsymbol{\sigma}_f$) under fully reversible loading were calculated using Basquin's equation for fatigue lives of 1×10^7, 1×10^8 and 1×10^9 cycles, as illustrated in **(Table 9)**, **(Table 10)** and **(Table 11)** present the results in order of the lowest and highest fatigue life achieved for the stress pair $\boldsymbol{\sigma}_a$ and $\boldsymbol{\sigma}_m$.

Table 9: Stress–life relationship estimated by Basquin's equation.

Material	Life (cycles)	σ_f (MPa)
DIN 34CrNiMo6	1×10^7	475
	1×10^8	436
	1×10^9	400
Al 6351 T6	1×10^7	174
	1×10^8	154
	1×10^9	136

Table 10: Results of partially reversible fatigue tests for the steel.

R	σ_a (MPa)	σ_m (MPa)	N_f (cycles)
-0.5	360	120	$1.31\times10^8 - 3.57\times10^8$
	450	150	$3.65\times10^5 - 5.22\times10^5$
-0.25	360	216	$5.97\times10^7 - 8.20\times10^7$
	400	240	$2.52\times10^5 - 4.87\times10^5$
0	315	315	$1.43\times10^6 - 3.40\times10^7$
	360	360	$2.43\times10^6 - 6.01\times10^6$

Table 11: Results of partially reversible fatigue tests for the aluminum alloy.

R	σ_a (MPa)	σ_m (MPa)	N_f (cycles)
-0.5	148	49	4.64×10^8 – run out
	111	37	run out
-0.25	148	89	$2.01\times10^7 - 7.20\times10^7$
	111	67	run out
0	148	148	$2.09\times10^6 - 1.40\times10^7$
	111	111	run out

For each material, three diagrams were constructed, each representing a specific fatigue life. Then, for each stress pair $\boldsymbol{\sigma}_a$ and $\boldsymbol{\sigma}_m$, the tests exhibiting the lowest fatigue life were selected to adopt a more conservative approach. Each test plotted in the diagram was evaluated to determine whether failure had occurred for the proposed fatigue life, with the objective of identifying and quantifying which models were able to predict potential fracture. **(Figure 15)** and **(Figure 16)** show the failure diagrams for both alloys.

To synthesize the results of **(Figure 15)** and **(Figure 16)**, Equation 11 presents the Evaluation of Model Accuracy (EMA):

$$EMA = \frac{|EF - FP|}{NT} x\ 100 \qquad 11$$

where EF is the number of experimentally obtained failures, FP is the number of failures predicted by the analyzed model and NT is the number of tests represented in the graph; in this study, NT equals 6. The results of each model within the FADs are presented in **(Table 12)**.

The Goodman model showed the best fit for both alloys, with errors below 16%, as expected, given its well-documented recurrent applicability in many engineering designs[39,55-57]. In parallel, analyzing the error values for the Gerber and Soderberg models in both alloys, the conservative Soderberg model was better suited for steel, whereas the aluminum alloy showed better agreement with the less conservative Gerber model. An investigation was conducted to evaluate the effect of microstructural inhomogeneities, since equivalence models are formulated purely based on mechanical parameters and do not account for the influence of metallurgical defects on fatigue behavior. The presence of heterogeneities was assessed using the methodology proposed by Wen-Jie P, et al.,[58] where Equation 12 determines a critical defect size capable of acting as a crack nucleation site.

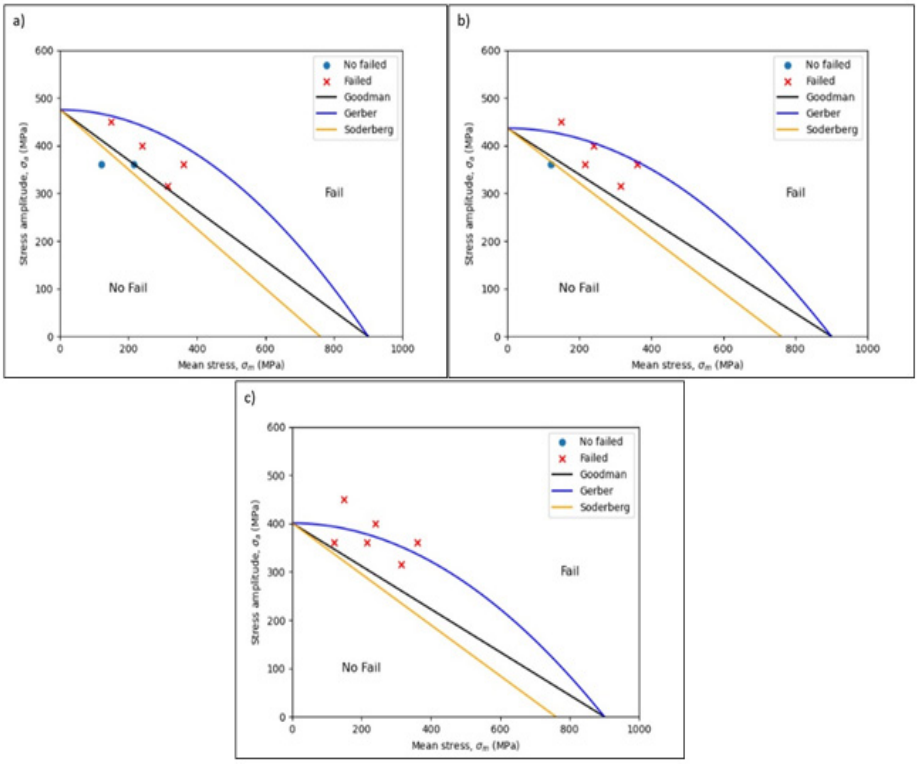

Figure 15: Failure diagram for the DIN 34CrNiMo6 steel: (a) Fatigue life of 1×10^7 cycles, (b) Fatigue life of 1×10^8 and (c) Fatigue life of 1×10^9

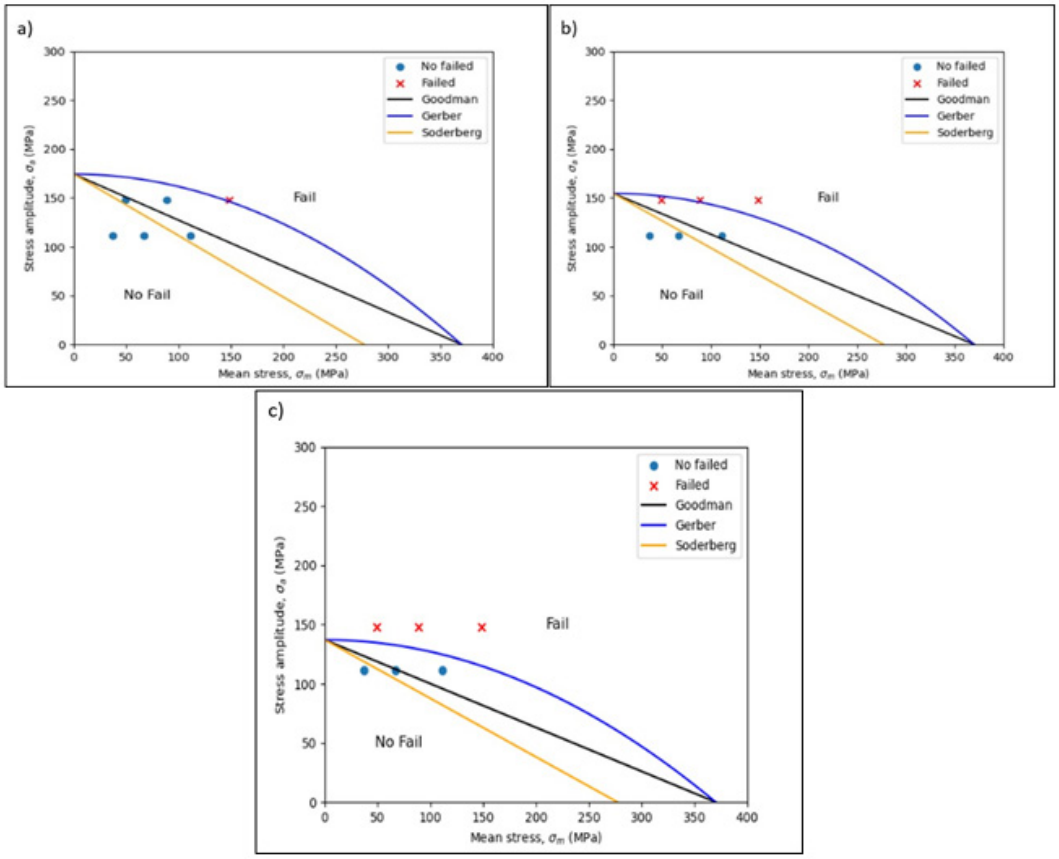

Figure 16: Failure diagram for the Al 6351 T6 alloy: (a) Fatigue life of 1×10^7, (b) Fatigue life of 1×10^8 and (c) Fatigue life of 1×10^9.

Table 12: Fatigue life prediction by equivalence models for DIN 34CrNiMo6 steel.

Life (cycles)	Models	EMA (%)
1×10^7	Goodman	0
	Soderberg	16
	Gerber	66
1×10^8	Goodman	0
	Soderberg	0
	Gerber	66
1×10^9	Goodman	0
	Soderberg	0
	Gerber	50

Table 13: Fatigue life prediction by equivalence models for Al 6351 T6 alloy.

Life (cycles)	Models	EMA (%)
1×10^7	Gerber	0
	Goodman	16
	Soderberg	50
1×10^8	Gerber	16
	Goodman	16
	Soderberg	16
1×10^9	Gerber	16
	Goodman	0
	Soderberg	33

$$\varphi_{inc}^{min} = C_{in}(1+\frac{120}{HV})6 \qquad 12$$

HV represents the Vickers hardness of the material and C_{in} is a coefficient dependent on the inclusion position, assuming values of 0.528 (subsurface), 0.813 (surface) and 0.969 (internal). To analyze the effect of inclusion size, the Gumbel distribution was applied, using the maximum likelihood method to determine the maximum inclusion size that can occur in each material[59]. A comparison between the maximum size of the inclusions estimated via Gumbel distribution (Gd) and the critical value calculated using Equation 12 is presented in **(Table 13)**.

Table 13: Assessment of the critical inclusion size in both alloys.

Material	**Vickers hardness (HV)**	**Gd** (μm)	**Position**	(μm)	**Gd status**
Al 6351 T6	105	21.01	surface	78.71	Below
			subsurface	51.12	Below
			internal	93.82	Below
DIN 34CrNi-Mo6	270	49.45	surface	7.38	Above
			subsuper-ficial	4.80	Above
			internal	8.80	Above

For the aluminum alloy, all evaluated inclusions exhibited dimensions below the critical size, regardless of their position. Therefore, crack nucleation in aluminum was predominantly driven by surface irregularities or local stress concentrations rather than the presence of inclusions. In contrast, for the steel, the maximum inclusion sizes exceeded the critical thresholds in all analyzed positions (surface, subsurface and internal). These results emphasize that inclusion size was a determining factor for fatigue behavior and for the evaluation of equivalence models within the failure diagram. In the aluminum alloy, failures occurred at longer lives, showing better predictability with the Gerber model, whereas the steel experienced premature failures due to inclusions exceeding the critical limit, aligning more closely with the Soderberg model.

Conclusion

The present study evaluated the applicability of classical stress equivalence models - Goodman, Gerber and Soderberg - in predicting the fatigue behavior of a high-strength structural steel (DIN 34CrNiMo6) and an aluminum alloy (Al 6351-T6) in the very high cycle fatigue regime, considering fully and partially reversible loadings. Besides this, this research emphasizes the importance of integrating mechanical modeling and microstructural characterization to achieve more robust and representative predictions of the fatigue life of metallic materials.

From the obtained results, one can draw the following conclusions:

- The Goodman model showed greater consistency in predicting fatigue life for both materials, highlighting its robustness for extrapolations beyond the conventional limit of 10^7 cycles. However, it was observed that the accuracy of the models depends significantly on microstructural factors.
- Nevertheless, it was observed that the accuracy of the Soderberg and Gerber models depends significantly on microstructural factors. With regards to the steel, the Soderberg model proved a more suitable match, mainly due to its more conservative nature, which more realistically reflected the influence of larger inclusions that exceeded the estimated critical size, resulting in premature failures.
- In contrast, for the aluminum alloy, whose inclusions remained below the critical threshold, the most appropriate prediction was obtained with the Gerber model, which is less conservative and provides a better fit for the alloy, where surface nucleation predominates and inclusions do not reach critical dimensions.
- These results reinforce that the validity of equivalence models in the VHCF regime cannot be assessed solely from the perspective of mechanical parameters, making it essential to consider microstructural heterogeneities, particularly those related to the size and distribution of inclusions.

References

1. Schijve J. Fatigue of Structures and Materials. Springer Netherlands 2008.
2. Suresh S. Fatigue of Materials. Cambridge University Press 1992.
3. Salvati E. Evaluating fatigue onset in metallic materials: Problem, current focus and future perspectives. Int J Fatigue 2024;188:108487.
4. Murakami Y. Metal Fatigue: Effects of Small Defects and Nonmetallic Inclusions. Elsevier Sci 2002.
5. Nadot Y. Fatigue from Defect: Influence of Size, Type, Position, Morphology and Loading. Int J Fatigue 2022;154:106531.
6. Zheng Z, Zhan M, Fu MW. Microstructural and geometrical size effects on the fatigue of metallic materials. Int J Mech Sci 2022;218:107058.
7. Yukitaka M, Masahiro E. Quantitative evaluation of fatigue strength of metals containing various small defects or cracks. Eng Fract Mech 1983;17(1):1-15.
8. Forrest PG. Fatigue of Metals. Pergamon 2013.
9. Dowling NE. Mechanical Behavior of Materials: Engineering Methods for Deformation, Fracture and Fatigue. Prentice Hall 1999.
10. Bathias. There is no infinite fatigue life in metallic materials. Fatigue Fract Eng Mater Struct 1999;22(7):559-565.
11. Pyttel B, Schwerdt D, Berger C. Very high cycle fatigue – Is there a fatigue limit? Int J Fatigue 2011;33(1):49-58.
12. Bathias C, Paris PC. Gigacycle Fatigue in Mechanical Practice. CRC Press 2004.
13. Mughrabi H, Antolovich SD. A tribute to Claude Bathias - Highlights of his pioneering work in Gigacycle Fatigue. Int J Fatigue 2016;93:217-223.
14. Wang Q, Khan MK, Bathias C. Current understanding of ultra-high cycle fatigue. Theor Appl Mech Lett 2012;2(3):031002.
15. Kazymyrovych V. Very high cycle fatigue of engineering materials: A literature review. Published online 2009.
16. Mason WP. Piezoelectric Crystals and Their Application to Ultrasonics... D. van Nostrand Company 1959.
17. Bathias C. Piezoelectric fatigue testing machines and devices. Int J Fatigue 2006;28(11):1438-1445.
18. Kanazawa, Nishijima. Stepwise S-N curve and fish-eye failure in gigacycle fatigue. Fatigue Fract Eng Mater Struct 1999;22(7):601-607.
19. Wang Q, Bathias C, Kawagoishi N, Chen Q. Effect of inclusion on subsurface crack initiation and gigacycle fatigue strength. Int J Fatigue 2002;24(12):1269-1274.
20. Wang Q, Berard J, Dubarre A, Baudry G, Rathery S, Bathias C. Gigacycle fatigue of ferrous alloys. Fatigue Fract Eng Mater Struct 1999;22(8):667-672.
21. Zhao P, Wang X, Yan E, et al. The influence of inclusion factors on ultra-high cyclic deformation of a dual phase steel. Mater Sci Eng A 2019;754:275-281.
22. Murakami Y. The effect of hydrogen on fatigue properties of metals used for fuel cell system. Int J Fract 2006;138(1):167-195.
23. Murakami Y, Nomoto T, Ueda T, Murakami Y. On the mechanism of fatigue failure in the superlong life regime (N> 107 cycles). Part 1: influence of hydrogen trapped by inclusions. Fatigue Fract Eng Mater Struct 2000;23(11):893-902.
24. Sakai T, Oguma N, Morikawa A. Microscopic and nanoscopic observations of metallurgical structures around inclusions at interior crack initiation site for a bearing steel in very high-cycle fatigue. Fatigue Fract Eng Mater Struct 2015;38(11):1305-1314.
25. Sakai T. Review and prospects for current studies on very high cycle fatigue of metallic materials for machine structural use. J Solid Mech Mater Eng 2009;3(3):425-439.
26. Shiozawa K, Lu L. Very high-cycle fatigue behaviour of shot-peened high-carbon–chromium bearing steel. Fatigue Fract Eng Mater Struct 2002;25(8-9):813-822.
27. Shiozawa K, Lu L, Ishihara S. S-N curve characteristics and subsurface crack initiation behaviour in ultra-long-life fatigue of a high carbon-chromium bearing steel. Fatigue Fract Eng Mater Struct 2001;24(12):781-790.
28. Furuya Y, Matsuoka S, Abe T, Yamaguchi K. Gigacycle fatigue properties for high-strength low-alloy steel at 100 Hz, 600 Hz and 20 kHz. Scr Mater 2002;46(2):157-162.
29. Ruben PM. Study of the fatigue strength in the gigacycle regime of metallic alloys used in aeronautics and off-shore industries. Published online 2010.
30. Dowling NE. Mean Stress Effects in Stress-Life and Strain-Life Fatigue. SAE Technical Paper 2004.
31. Sendeckyj GP. Constant life diagrams - a historical review. Int J Fatigue 2001;23(4):347-353.

32. Schütz W. A history of fatigue. Eng Fract Mech 1996;54(2):263-300.
33. Goodman J. Mechanics Applied to Engineering. Longmans, Green 1919.
34. Gerber W. Bestimmung Der Zulässigen Spannungen in Eisen-Constructionen. Wolf 1874.
35. Soderberg CR. Factor of safety and working stress. Trans Am Soc Mech Eng 1930;52(2):13-21.
36. Wöhler A. *Über* Die Festigkeitsversuche Mit Eisen Und Stahl. Ernst & Korn 1870.
37. Haigh BP. Experiments on the fatigue of brasses. J Inst Met 1917;18(2):55-86.
38. British Standards Institution. Guide to Methods for Assessing the Acceptability of Flaws in Metallic Structures. British Standards Institution 2005.
39. Toasa Caiza PD, Sire S, Ummenhofer T, Uematsu Y. Low-cost estimation of Wöhler and Goodman-Haigh curves of Ti-6Al-4V samples by considering the stress ratio effect. Fatigue Fract Eng Mater Struct 2022;45(2):441-450.
40. Maxwell DC, Nicholas T. A rapid method for generation of a Haigh diagram for high cycle fatigue.
41. Karnati AK, Sarkar A, Nagesha A, et al. Evaluation of high cycle fatigue behaviour of alloy 617M at 973 K: Haigh diagram and associated mechanisms. Int J Press Vessels Pip 2019;172:304-312.
42. Bellows RS, Muju S, Nicholas T. Validation of the step test method for generating Haigh diagrams for Ti–6Al–4V. Int J Fatigue 1999;21(7):687-697.
43. Pallarés-Santasmartas L, Albizuri J, Avilés A, Avilés R. Mean Stress Effect on the Axial Fatigue Strength of DIN 34CrNiMo6 Quenched and Tempered Steel. Metals 2018;8(4):213.
44. Ponnapureddy S, Sarkar A, Nagesha A, Narasaiah N, Srinivasa Rao B. A re-visit to the Haigh diagram with the effect of creep damage on the high cycle fatigue behavior of alloy 617M. Int J Fatigue 2021;149:106258.
45. Standard Test Methods and Practices for Chemical Analysis of Steel Products 2025.
46. E01 Committee. Test Method for Analysis of Aluminum and Aluminum Alloys by Spark Atomic Emission Spectrometry.
47. E28 Committee. Test Methods for Tension Testing of Metallic Materials.
48. E28 Committee. Test Method for Youngs Modulus, Tangent Modulus and Chord Modulus.
49. E04 Committee. Test Method for Microindentation Hardness of Materials.
50. E04 Committee. Guide for Preparation of Metallographic Specimens.
51. E04 Committee. Practice for Determining the Inclusion or Second-Phase Constituent Content of Metals by Automatic Image Analysis.
52. Teixeira MC, Brandão ALT, Parente AP, Pereira MV. Artificial intelligence modeling of ultrasonic fatigue test to predict the temperature increase. Int J Fatigue 2022;163:106999.
53. Davis JR, Associates JRD, Committee ASMIH. Aluminum and Aluminum Alloys. ASM International 1993.
54. Clara Carvalho Teixeira M. Fatigue Failure Assessment in Ultrasonic Test Based on Temperature Evolution and Crack Initiation Mechanisms. PhD in Materials Engineering and Chemical and Metallurgical Processes. Pontifical Catholic University of Rio de Janeiro 2023.
55. Zhang Z, He Z, Yang B, et al. An improved Goodman-Smith fatigue limit diagram for railway vehicle base metals and welded structures. Int J Fatigue 2024;182:108160.
56. Martinez-Puente E, Llavori I, Muñiz-Calvente M, Penalba M. Impact of mean stress on mooring line fatigue assessment: An analytical study. Ocean Eng. 2025;324:120621.
57. Silva BL da, Ferreira JL de A, Oliveira F, Araújo JA. Influence of mean stress on the fatigue strength of ASTM A743 CA6NM alloy steel. Fract Struct Integr 2010;4(14):17-26.
58. Wen-jie P, Huan X. The influential factors on very high cycle fatigue testing results. In: MATEC Web of Conferences. Vol 165. EDP Sciences 2018:20002.
59. Calculation of the Fatigue Limit of High-Strength Steel Specimens at Different Loading Conditions Based on Inclusion Sizes - Schumacher - 2021 - steel research international - Wiley Online Library 2021.